Materials & Design 225 (2023) 111507

Contents lists available at ScienceDirect

Materials & Design

journal homepage: www.elsevier.com/locate/matdes

Electrical anisotropy controlled heating of acrylonitrile butadiene styrene 3D printed parts

Liberata Guadagno [a,*], Francesca Aliberti [a], Raffaele Longo [a], Marialuigia Raimondo [a], Roberto Pantani [a], Andrea Sorrentino [b], Michelina Catauro [c], Luigi Vertuccio [c,*]

[a] Department of Industrial Engineering, University of Salerno, Via Giovanni Paolo II, 84084 Fisciano, Salerno, Italy
[b] Institute for Polymers, Composites, and Biomaterials (IPCB-CNR), via Previati n. 1/E, 23900 Lecco, Italy
[c] Department of Engineering, University of Campania "Luigi Vanvitelli", via Roma 29, I-81031 Aversa, Italy

HIGHLIGHTS

- Fused Filament Fabrication (FFF) 3D Printed artefacts were designed with different multi-scale configurations of the internal conductive pathways.
- Electrothermal conduction paths through the sample were controlled by changing the printing parameters.
- Tunneling Atomic Force Microscope (TUNA) provides direct information on the electrically conductive paths essentially composed of aligned Carbon Nanotubes.
- The raster angle affects the electrical conductivity of the artefact printed parts and their heating.

GRAPHICAL ABSTRACT

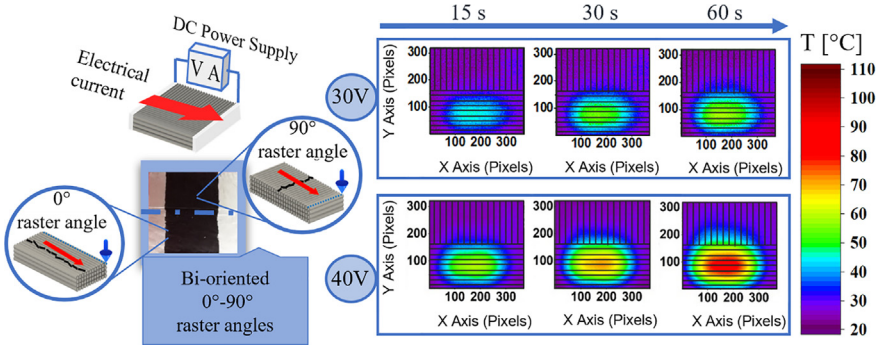

ARTICLE INFO

Article history:
Received 24 August 2022
Revised 12 December 2022
Accepted 13 December 2022
Available online 14 December 2022

Keywords:
3D printing composites
Electrical properties
Joule effect
Self-heating element

ABSTRACT

This study proposes a simple method to produce three-dimensional (3D) manufacts with multiscale configurations and controlled electrical resistivity. 3D printed artefacts, based on acrylonitrile butadiene styrene and carbon nanotubes (CNTs), are obtained by fused filament fabrication. Highly orientated conductive pathways are achieved in the sample by selecting appropriate printing parameters. Scanning electron microscopy and tunnelling atomic force microscopy confirm that the conductive traces are essentially composed of aligned CNTs. The printing process determines an increase in the electrical conductivity from 6.88×10^{-2} (spooled filament) to 11.9 S/m (printed filament). The orientation of the spatial domains from the macro- to nanoscale is responsible for a decrease in the electrical resistance from 7782 (90° raster angle sample) to 478 Ω (0° raster angle sample). Appropriate selection of the configuration and dimensions of electrical contacts confers the ability to selectively heat the part when subjected to an electric source. Temperature differences up to 55 °C were obtained in samples printed with a double-angle raster combination by changing the applied voltage from 20 to 40 V. This strategy can be used to fabricate electronic devices, thermistors capable of converting electrical energy to thermal energy, heat exchangers, and shielding for electromagnetic interference in a single step.

* Corresponding authors.
E-mail addresses: lguadagno@unisa.it (L. Guadagno), luigi.vertuccio@unicampania.it (L. Vertuccio).

https://doi.org/10.1016/j.matdes.2022.111507
0264-1275/

1. Introduction

New technologies for processing materials, called additive manufacturing (AM), have recently captured the interest of an increasing number of industries and academics because of their ability to produce complex three-dimensional (3D) components by adding material layer by layer instead of removing it. AM can provide digital flexibility and efficiency to manufacturing operations [1]. AM includes a group of advanced manufacturing technologies that allow flexible production of precise structures with highly complex shapes that are complicated to manufacture using conventional methods such as machining, casting, and injection moulding [2,3]. The most popular AM technologies today are categorised as vat photopolymerisation, material jetting, binder jetting, powder bed fusion, direct energy deposition, sheet lamination, and material extrusion. Their differences arise from the different types of processed materials, from thermoplastic and thermosetting polymers to metal alloys and ceramic materials [2]. The final properties of the printed part depend on the starting material used and the processing conditions. AM is widely used with pristine (unfilled) materials; however, both academic and industrial research is moving towards extending these technologies to composite materials, particularly nanocomposite materials. Nanocomposite materials have innumerable advantages over pristine materials. It has been demonstrated that adding nanoparticles to a matrix improves or completely changes the final properties of the material with respect to those of the initial material. By appropriately choosing the type of nanofiller, the interfacial properties can be studied and modelled to tune the macroscopic properties, such as the thermal and electrical conductivity, of the final composite material [4]. Furthermore, process parameters can be exploited to improve the new characteristics provided by nanoparticles in the nanocomposite item according to the application field. Factors such as the electrical conductivity of metal alloys and ceramic materials are affected by the matrix structure [5,6] or the conductive filler weight fraction [7]. The fused filament fabrication (FFF) approach is generally used with thermoplastic polymers. FFF 3D-printed items are applied in the aeronautical [8–10], mechanical engineering [11–13], medical [14–19], electronic [3,20,21], and civil fields [22].

A typical disadvantage of polymeric (FFF) 3D-printed parts is their poor mechanical properties if used as load-bearing or load-bearing self-responsive parts of industrial components. These drawbacks significantly limit the application of the AM polymeric materials in some industrial sectors. It is well known that the presence of nanoparticles dispersed in polymeric matrices allows for the manufacture of composites with functional properties and a mechanical performance that are not attainable with the polymeric matrix alone [23–26]. Furthermore, the rheological and curing kinetics can be modified [27,28]. The combination of nanotechnologies with 3D printing provides significant opportunities for the production of 3D materials with optimised properties and functionality [29–33], including polymers such as acrylonitrile butadiene styrene (ABS) [34,35], polylactic acid (PLA) [36–40], nylon, and polypyrrole [41]. Among the different printing techniques (stereolithography and 3D plotting, inkjet 3D printing, selective laser sintering, and others), FFF printers are the most used for prototyping, especially when thermoplastic polymers with low melting temperatures, such as ABS, PLA, and thermoplastic polyurethane, are considered. The features of printed parts can be controlled by tuning parameters such as the printing path, layer thickness, raster angle, air gap, and raster width [42]. Anisotropy and voids can be eliminated by accurately controlling the printing parameters, making printed polymer nanocomposites suitable for the desired application [43]. For example, a different printing path leads to a different thermal conductivity of graphene-based nanocomposites [44] owing to the graphene orientation and distribution of voids, which hinder efficient heat conduction. Similar results were obtained using graphene nanoplatelets in printable polyamide (PA12) [45], where the as-printed composite parts exhibited significantly higher thermal conductivity and mechanical properties than the compression-moulded parts. When employing carbon nanotubes (CNTs), orientation effects can influence parameters ranging from the frictional behaviour of the CNTs under different sliding conditions [46] to the thermal conductivity of the composites [47]. Therefore, depending on the processing conditions, 3D-printed parts clearly show a certain degree of anisotropy, which negatively affects their final properties. Not surprisingly, most scientists in this field have studied methods to eliminate anisotropy in the resulting physical properties of 3D-printed parts and, consequently, have enhanced the reproducibility of the final properties. However, it is also true that if specific anisotropies are well-controlled and programmed at the printing stage, they can become highly desired peculiarities, capable of opening new interesting applications. For example, lightweight parts free from metallic wires can be designed to be conductive in specific directions and insulating in other directions or capable of exhibiting different mechanical or thermal conduction properties depending on the chosen direction throughout the sample. Accordingly, the literature shows that the AM method is one of the best strategies to confer anisotropic functionalities to 3D-printed parts. Dul *et al.* performed a comparative investigation of the effects of different percentages of multiwalled CNTs (MWCNTs) and single-walled CNTs (SWCNTs) on the electrical resistivity of 3D-printed parts manufactured using ABS nanocomposites [48]. The authors found that the resistivity values in the XY direction for all ABS/CNT 3D-printed parts were lower than those in the Z direction.

AM can be applied to produce heating systems using electrothermal phenomena based on the "Joule heating" effect. CNT-nanocomposites of PA 12 [49] and PLA [50] or composite fibres of polyacrylonitrile [51] were found to exhibit excellent potential as polymeric conductive materials for thermoelectrical applications. In other cases, the Joule heating phenomenon was exploited to heal damaged sites using Diels-Alder-based polymer nanocomposites [52]. The present study explored the capability of FFF to create 3D-printed parts with customised anisotropic properties based on orientated nanometric networks. Different multiscale configurations were prepared using FFF 3D printing of artefacts composed of ABS with MWCNTs. Scanning electron microscopy (SEM) and tunnelling atomic force microscopy (TUNA) were employed to verify the controllability of the conductive paths in the spatial domain from the macro- to nanoscale. FFF 3D printing experiments and sample characterizations demonstrated that the choice of appropriate printing parameters allows for the electrothermal conduction paths to be controlled to achieve different controlled temperatures in several areas of the printed sample. Therefore, by using the anisotropy of the resistivity value of 3D-printed parts, it was demonstrated that these parts can be heated in a controllable manner. A relevant study result is that the raster angle is the dominant factor for changing the conductivity of the parts, and consequently for controlling heat generation along the same element when subjected to a unique electric potential difference.

The adopted methodology results in a very promising strategy for preparing functional materials for use in electronic devices or as multilayer materials, where the active layer is functional for different scopes, namely, to activate self-healing regions more prone to damage using heat or to induce changes in the shape of parts embedded in shape-memory metal wires. In this manner, it is possible to create preferential heat flow in predetermined directions,

as defined in the CAD modelling step. Such a solution can contribute to efficiently designing samples with the inherent ability to differentiate the heating responses depending on the spatial zone placement and the function to which it is assigned.

2. Experimental section

2.1. Preparation of FFF 3D-printed samples

ABS filled with CNTs, supplied by 3DXTECH Additive Manufacturing, was used in the form of filaments (1,75 mm diameter) to fabricate the electrically conductive parts. In Fig. S1.1 of the supplementary information (S.I.), thermogravimetric curves show that the concentration of CNTs was approximately 8 % wt/wt.

Fig. S2 shows the FTIR spectrum of the ABS-CNT sample, which exhibited all the expected signals. Table 1 lists the 3D printing parameters used for the test specimens.

The commercial material loaded with 8 % wt/wt of CNTs fulfils two essential requirements related to the production and properties of printed parts. The ABS matrix was selected because this amorphous copolymer allows higher operating temperatures than the most used printable material, PLA, because of its glass transition temperature (Tg) (approximately 110 and 60 °C for ABS and PLA, respectively). Additionally, ABS is the material with which about 90 % of all prototypes are produced using FFF, particularly in clinical and automotive applications [53].

It has been reported that CNT concentrations > 10 % wt/wt are not appropriate to achieve a good compromise between nanocomposite 3D-processability and mechanical–electrical properties [54]. The selected CNT concentration of 8 % wt/wt was sufficient to obtain a sample beyond the electrical percolation threshold, which guarantees good electrical conductivity and efficient Joule heating without compromising the printing of composites based on ABS.

All CAD files were generated using 3DBuilder and exported as (.stl) files, which were then imported into Slic3r Prusa Edition (Prusa Research). A custom configuration file (.gcode) was created to set the deposition direction for each successive layer. All tests were performed using an Original Prusa i3 MK2 3D printer (Prusa Research). The deposition width was set to 450 μm and the overlap between the infill and perimeters to 25 %. The raster angle, which is the nozzle angle between the path and the X-axis of the printing platform, is one of the relevant parameters in the FFF 3D printing method. In the first stage of this study, two samples with two different printing raster angles were fabricated to determine the effect of patterning on the heating performance. In particular, the infill pattern was straight for both samples, whereas the raster angle was 0° for the horizontally-orientated printed sample and 90° for the vertically-orientated printed sample (see Fig. 1). Both printed samples were composed of 17 overlapped layers with a resulting thickness of 3.4 mm. Fig. 1(a, c), in which the 3D model is sliced using Slic3r software, shows the raster angle on each layer during the printing parameter setting. The optical images in Fig. 1 (b, d) show the deposition direction.

Table 1
3D printing parameters used for the production of the ABS composite specimens.

Parameters	Specifics
Nozzle diameter	0.4 mm
Layer thickness	0.2 mm
Infill density	100 %
Platform temperature	80 °C
Extrusion temperature	250 °C
Printing speed	80 mm/s
Raster angle	0° and 90°

It is important to note that these two samples were printed with the same infill density (100 %, see Table 1); therefore, any differences in the experimental results depend only on the orientation of the extruded filament deposition.

2.2. Methods

2.2.1. Joule heating tests

A data logger (TC-08 supplied by Pico Technology) was used to acquire the thermocouple measurements. The temperatures were measured using dedicated LabVIEW software and thin wire thermocouples (Type K, Omega Engineering ltd.) with negligible thermal inertia located at the centre of the sample (see Fig. 2(b, e)). A laboratory power supply (EA-PSI 8360–10 T. Elektro-Automatik, 0–360 V, 0–10 A, 1000 W max) was connected to the short sides of the samples (dimensions 0.35 × 9.0 × 4.5 cm^3), which were coated with an approximately 50 μm-thick silver paint (Fig. 2(b, e)) with a surface resistivity of 0.001 Ω·cm to ensure ohmic contact with the measuring electrodes. Each heating test was performed at a constant voltage until the steady-state condition was reached (1200 s). The samples were maintained in a fixed position in contact with air at 25 °C on both sides.

A thermal infrared camera (Fluke Ti401 Pro Thermal Imager, WA, USA; spatial resolution IFOV = 0.93 mRad, thermal sensitivity NETD ≤ 0.075 °C) was used to capture the heating maps on the sample surface, from which the temperature distribution was obtained.

2.2.2. Electrical and thermal conductivity

The electrical conductivity was measured keeping the samples at 25 °C using a two-probe method on rectangular specimens (0.35 × 9.0 × 4.5 cm^3) using the equipment and procedures described in Ref. [55]. The contact resistance was considered negligible because the measured electrical resistance was on the order of kΩ.

The thermal conductivity was determined using a method for samples with rectangular or cylindrical macroscopic shapes. In this method, the sample of interest is positioned on a heat source (plate). The thermal conductivity can be determined by monitoring the heat flow through the sample and the temperatures of the two opposite surfaces (one of which is exposed to the heat source). The thermal conductivity (k) of the samples was calculated using the inverse formula of the Fourier equation under stationary conditions, as shown in Eq. (1).

$$k = q * \delta/(T_h - T_c) \quad (1)$$

where q is the effective thermal flow passing through the sample, δ is the thickness of the sample whose conductivity is to be measured, and T_h and T_c are the "hot source" and "cold source" temperatures, respectively. A heat flow meter (FHF01-02 provided by HUKSEFLUX) allows for the effective thermal flow inside the sample to be calculated and contains a special K-type thermocouple used to measure the sample temperature.

2.2.3. Morphological characterisation

SEM micrographs of the samples were acquired using the equipment and procedures described in Ref. [24]. Before the SEM investigation, the printed samples were subjected to a procedure to remove part of the polymeric matrix using an oxidising solution (etching solution). The etching reagent was prepared by stirring 1.0 g potassium permanganate in a mixture of 95 ml sulfuric acid (95–97 %) and 48 ml orthophosphoric acid (85 %). The samples were immersed in the fresh etching reagent at room temperature and agitated for 24 h. The samples were subsequently washed using a cold mixture of two parts by volume of concentrated sulfuric acid and seven parts of water. The samples were then washed with 30 % aqueous hydrogen peroxide to remove any manganese

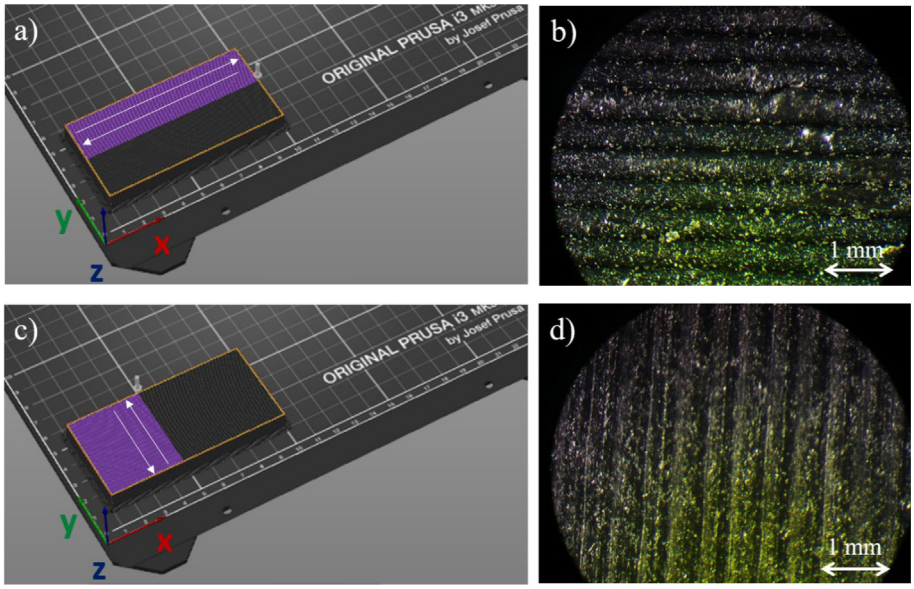

Fig. 1. (a) Preview of the 0° raster angle extruded filament deposition, (b) optical image showing the deposition direction of the sample with a 0° raster angle, (c) preview of the 90° raster angle extruded filament deposition, and (d) optical image showing the deposition direction of the sample with a 90° raster angle.

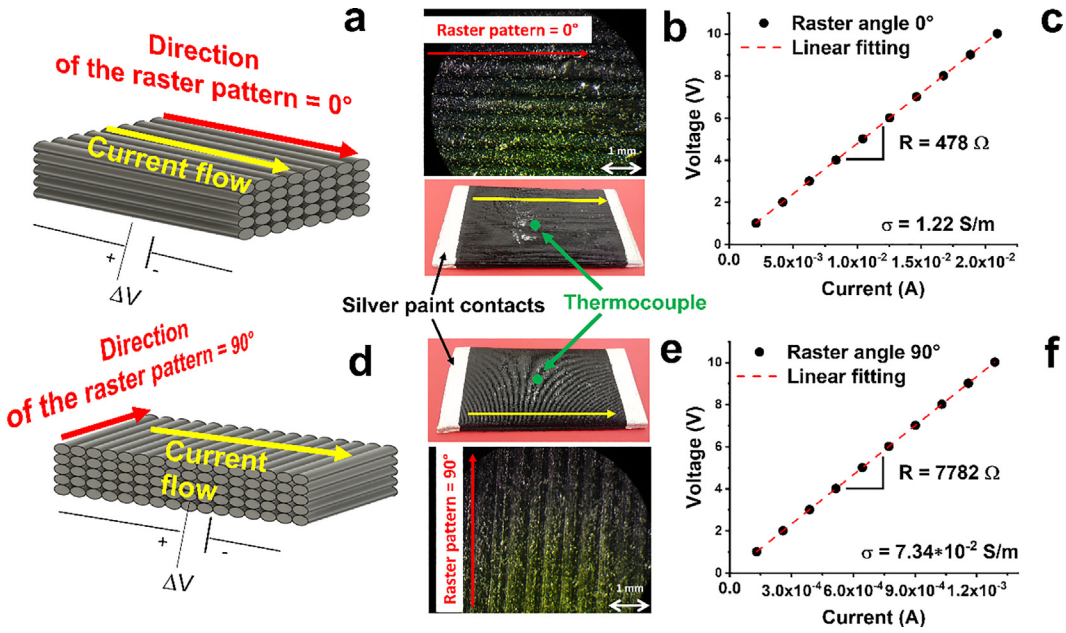

Fig. 2. (a, d) Configurations of the deposition direction, (b, e) photograph and optical image of the samples, (c) voltage versus current behaviour of the system printed with a raster angle of 0°, and (f) voltage versus current behaviour of the system printed with a raster angle of 90°.

dioxide. The samples were finally washed with distilled water and maintained under vacuum for 2 d. The areas and points of each printed sample subjected to SEM investigation are marked with red squares and arrows in Figs. 3(a), 4(a), and 5(a). TUNA current images were recorded using a DC sample bias of 3 V and current sensitivity of 1 pA/V. The scan rate was 0.500 Hz. The number of sample lines per rump was set at 512. The integral gain was 2.000 and the proportional gain was 5.000. The TUNA current images were examined using NanoScope Analysis 1.80 (Build R1.126200; Bruker). The etching treatment used for the SEM investigation was also adopted for the samples subjected to the TUNA current investigations.

3. Results and discussion

3.1. Characterisation of 3D parts

3.1.1. Electrical and heating properties

Two different printing raster angles were adopted to evaluate the effect of the extruded filament deposition direction on the electrical and heating properties of the prepared 3D parts. Constant voltage was applied to both the rectangular samples in the same direction to make the direction of the current flow parallel and perpendicular to the extruded filament deposition direction, respectively, as illustrated in Fig. 2(a, d). A raster angle of 0° indicates a

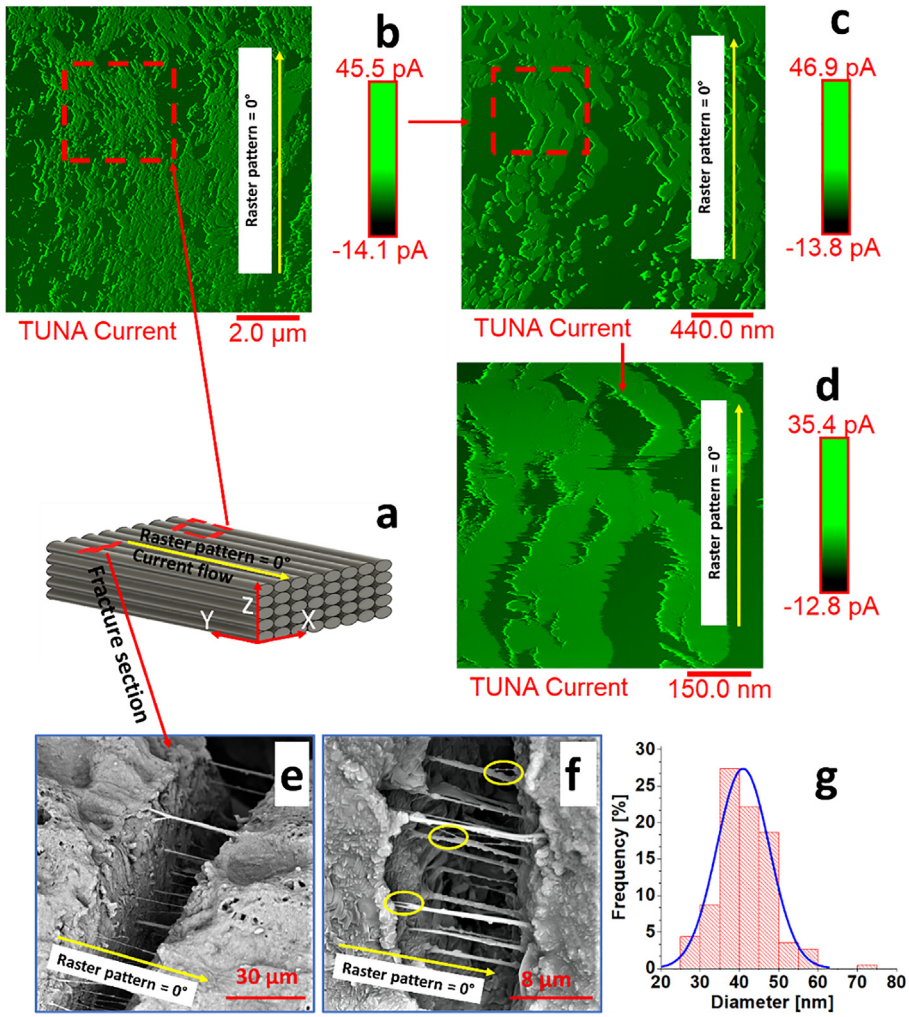

Fig. 3. (a) Schematic diagram of the sample in which the investigated surface (red square in Fig. 3(a)) is parallel to the XY plane, (b–d) TUNA current images at increasing magnifications (following the direction of the arrow) of the investigated surface, (e, f) SEM images of the fracture section on the investigated surface, and (g) distribution of the bare MWCNT diameters. (For interpretation of the references to colour in this figure legend, the reader is referred to the web version of this article.)

filament deposition direction that is parallel to the direction of the current flow (see Fig. 2(a)), and a raster angle of 90° indicates a filament deposition direction that is normal to that of the current flow (see Fig. 2(d)). Both printed parts were composed of 17 overlapped layers with a resulting thickness of 3.4 mm.

The DC volume conductivity of the two configurations was measured. Fig. 2(c, f) shows the results of the voltage-current measurements. The electrical resistance was obtained from the slope of the linear fit of the experimental data. The deposition direction of the filled ABS strongly affected the measured resistance, which was 478 Ω for the raster angle of 0° and 7782 Ω for the raster angle of 90°. This considerable difference was attributed to the different electrical interconnections between the CNTs in the two configurations. A higher number of electrical interruptions occurred at a raster angle of 90°, as compared to the case in which the deposition follows the direction of the current flow, as happens for the 0°-orientated filaments.

3.1.2. Correlation between electrical/heating properties and morphological characteristics

Figure 3(b–d) shows TUNA current images at increasing magnifications (following the direction of the red arrow) of the chemically-etched sample surface. The etching treatment was performed according to the method described in Ref. [56]. The AFM-TUNA technique is a powerful tool for investigating micrometric/-nanometric electrically conductive paths that interpenetrate the insulating spatial domains emerging on the surface of the higher layer under observation. In Fig. 3(b–d), the colour of the lateral scale bar allows for the rapid investigation of the morphological features and the extended conductive paths on the sample surface. A lighter colour tone characterises the spatial region with higher electrical conductivity. The extruded filament deposited (after passing through the nozzle) in the tests described here is characterised by an ellipsoidal section, with a long and short axes of approximately 400 and 200 µm, respectively.

Considering that the outer diameter range of the MWCNTs is 23–63 nm, it is evident in Fig. 3(b–d) that the lighter-coloured traces correspond to the conductive paths and can be identified as MWCNTs, and tended to be orientated in the direction of the 0° raster pattern (yellow arrow in Fig. 3(a)).

Hence, the TUNA current investigation confirmed that the CNTs were tendentially aligned with the long axis in the direction parallel to the direction of the 0° raster pattern. Fig. S3 (of S.I.) shows TUNA current images of the two different zones of the spooled filament before the printing process. The sample was conductive because of the presence of CNTs; however, no preferentially orientated electrically conductive paths were detected in the TUNA current image of the spooled sample.

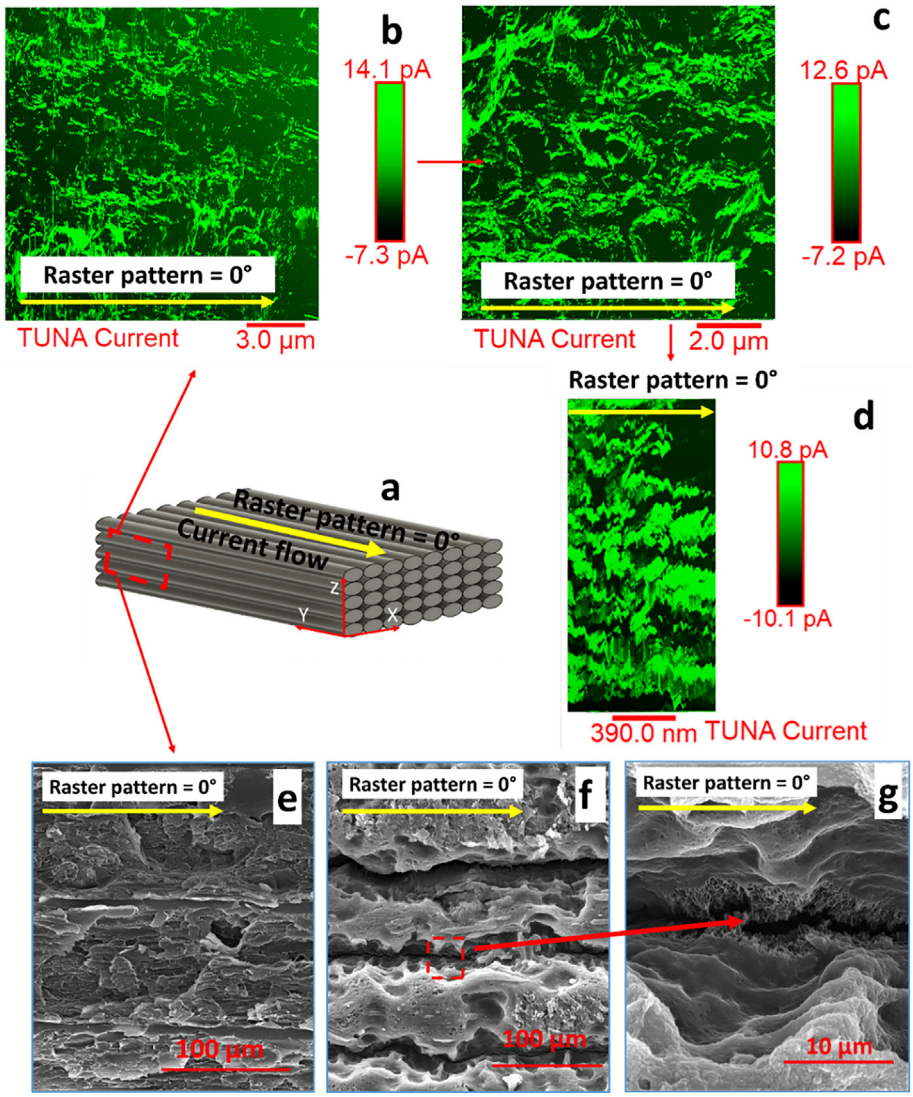

Fig. 4. (a) Schematic diagram of the sample in which the investigated surface (red square in Fig. 4(a)) is parallel to the YZ plane, (b–d) TUNA current images at increasing magnifications (following the direction of the arrow) of the investigated surface. SEM images of the (e) unetched and (f, g) etched surfaces at increasing magnifications. (For interpretation of the references to colour in this figure legend, the reader is referred to the web version of this article.)

The detected CNT alignment along the printed filament clearly explains the considerable difference in the electrical conductivity between the single spooled filament (before 3D printing) and the single printed filament (after 3D printing). It was determined that the electrical conductivity of the printed filament (11.9 S/m) is approximately-two orders of magnitude higher than that of the spooled filament (0.0688 S/m). The values are reported in Table 2 and are commented upon later in the text.

The sample schematically illustrated in Fig. 3(a) was damaged by slightly bending the printed sample at cryogenic temperatures (in liquid nitrogen), demonstrating a fracture perpendicular to the direction of the 0° raster pattern.

SEM images were then acquired in the damaged region of the sample after the etching treatment (Fig. 3(e, f)) to more accurately explore the arrangement of the nanofiller inside the filaments. It was evident that the soft etching only acted effectively on the polymer matrix, leaving most of the CNTs undamaged. The CNTs appeared to function as reinforcing ropes between the two damaged surfaces in the fracture section. Furthermore, the CNTs appeared well orientated in the same direction, which is parallel to the direction of the 0° raster pattern, confirming the results in the TUNA current mapping images. It is worth noting that, the CNTs in the fraction section appeared to be strongly anchored to a layer of the polymer matrix due to the mild etching, and in some cases, was composed of more than one nanotube (yellow ellipses in Fig. 3(f)), as also deduced from the diameter of the ropes.

The diameter of the ropes, excluding the case where more MWCNTs were overlapped or intertwined (evident in the studied images), ranged between 183 and 792 nm. Hence, it is possible to observe a different thickness of the matrix layer along the MWCNTs, resulting in a local assembly similar to that of beads. The thickness of the polymeric coating around the MWCNTs can be approximated by comparing the thickness of the ropes (in the fracture section) with the thickness distribution of the bare MWCNTs. The diameter distribution of the bare MWCNTs, shown in the histogram in Fig. 3(g), was obtained after an intense etching procedure to almost completely remove the polymeric layer adhering to the MWCNT walls.

Fig. 4 shows a schematic diagram of the section normal to the printed filament deposition (red square in Fig. 4(a)), TUNA current images at increasing magnifications (following the direction of the arrow) (Fig. 4(b–d)), SEM image of the unetched section (Fig. 4(e)),

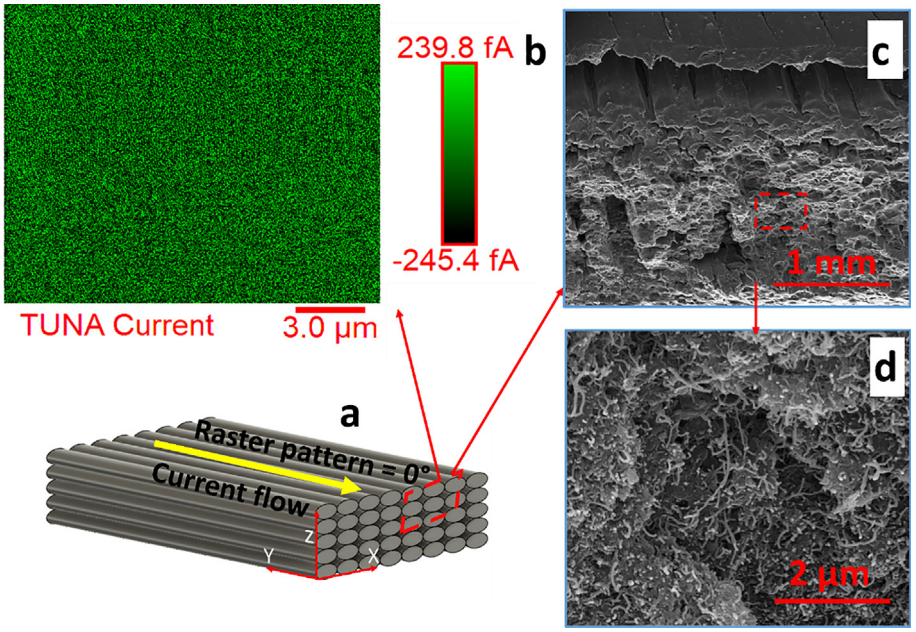

Fig. 5. (a) Schematic diagram of the sample in which the investigated surface (red square in Fig. 5(a)) is parallel to the XZ plane, (b) TUNA current image and (c, d) SEM images at different magnifications of the investigated surface (red square) parallel to the XZ plane. (For interpretation of the references to colour in this figure legend, the reader is referred to the web version of this article.)

and SEM images of the etched section at increasing magnifications (Fig. 4(f, g)) after being broken in liquid nitrogen. The TUNA current images correspond to the unetched sample sections as it allowed for the arrangement of the CNTs and the layer along the normal section of the sample (red squares) to be better investigated. The TUNA current images clearly show jagged bands of conductive regions that run almost parallel to the direction corresponding to a raster angle of 0°. A statistical investigation of the width of these bands shows that they present a size of approximately 200 nm. However, owing to the jagged bands, the dimensions along each band also reached a value of approximately 250 nm, demonstrating that bundles of CNTs run in the same direction. This observation was corroborated by the SEM image of the section shown in Fig. 4(f). It is worth noting that an intense etching procedure was performed before the acquisition of the SEM image of the sample shown in Fig. 4(g, f). Fig. 4(g) shows a magnified image of the region between the layers of filaments. In the centre of the image (red arrow), CNTs can be clearly seen emerging from two adjacent layers. This observation was possible because the chemical etching performed on the samples shown in Fig. 4(f, g) preferentially consumed the polymer between the filament layers, as can be deduced by comparing the SEM image of the sample in Fig. 4(e) (not etched) with the images of the etched samples (Fig. 4(f, g)).

Fig. 5 shows SEM images (Fig. 5(c, d)) at different magnifications of the other section normal to the deposition of the filaments (red square in the schematic diagram of Fig. 5(a)) and the corresponding TUNA current image (Fig. 5(b)) of the printed ABS composite.

The TUNA current image clearly exhibits homogenous conductivity. In this case, the clearest regions (seen almost as clear points) correspond to CNTs (seen in their section perpendicular to their long axis).

The regions of the conjunction between the fused printed filaments can be seen in the SEM images in Fig. 5(c, d). Fig. 5(d) shows a magnified image of the red square in Fig. 5(c), which was captured between two different fused filaments belonging to the same layer (on the plane parallel to the sample surface). Despite the intense etching procedure described in section 2.2.3, different CNTs appeared to be placed between different filaments (see the SEM image of the sample in the XZ plane).

However, the lower compactness of the material between parallel filaments, as compared to that detected along a filament alone, is clearly visible. This also reduces the number of electrical contacts between nanotubes belonging to adjacent filaments. Furthermore, as observed in the TUNA current and SEM images in Figs. 3 and 4, most CNTs were preferentially aligned along the long axis of the same printed filament. They locally appeared as singularly aligned (see Fig. 3(e)) or densely intertwined bundles that appear to follow the direction of filament deposition (see Fig. 3(c)).

The absence of the alignment phenomenon in the direction perpendicular to the long axis of the filament and the presence of electrical interruptions in the current flow along the direction normal to the deposition of the filament well explains the different electrical resistance values obtained in the two considered configurations (raster angles of 0 and 90°). Along the direction of the deposited filament, the electrical current flows without interruptions; vice versa, between one filament and the other, the current explores many paths not electrically interconnected.

The electrical conductivity of the printed samples was investigated and compared to that of a sample obtained by finely treating cut pieces of spooled filaments between the plates of a hot press at 210 °C for 15 min. This comparison validates the assumption that the printing process affects the arrangement of the conductive nanotube network along the filaments and the interruptions between them. Films with a thickness of 0.32 mm were obtained (see Table 2). Table 2 compares the electrical conductivity of the obtained specimens. The electrical conductivity of the single spooled filament (before crossing the nozzle), where no preferential conductive paths are observed (see section 3 of the S.I.), was also included in the table for comparison. The electrical conductivity of this filament, as compared to that of the single printed filament, clearly demonstrated that the extrusion of the spooled filament through the nozzle caused strong changes in the arrangement of the nanofiller along the printed filament, causing a preferential orientation of the nanotubes along the direction of the deposited filament (as also observed in the TUNA current images

Table 2
Electrical conductivity of the ABS composites: spooled filament, printed filament, 3D-printed composites, and film composite.

Specimen	Electrical Conductivity (S/m)
Single spooled filament 	6.88×10^{-2}
Single printed filament 	1.19×10^{1}
3D-printed composite (Raster angle of 0°) 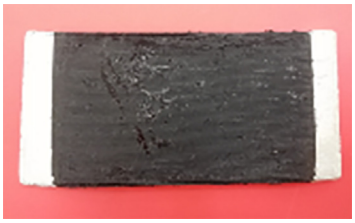	1.22
3D-printed composite (Raster angle of 90°) 	7.34×10^{-2}
Composite film 	2.42×10^{-2}

in Fig. 3 and 4). The electrical conductivity of the single printed filament was two orders of magnitude higher than that of a single spooled filament (173 times higher). The higher shear stresses in the thin printing nozzle resulted in an increase in the conductivity from 6.88×10^{-2} to 11.9 S/m.

The difference in electrical conductivity between the 0°- and 90°-orientated samples was two orders of magnitude, that is, 1.22 and 7.34×10^{-2} S/m, respectively.

The electrical conductivity comparison between the 3D-printed with a raster angle of 0°, 3D-printed with a raster angle of 90°, and compression moulded composites indicated that the difference in the electrical conductivity between the two configurations of the printed specimens is not attributable only to the absence of a high number of electrical contacts in the normal direction to the deposition of the material. Indeed, the film specimen without voids exhibited an electrical conductivity value of the same order of magnitude as that of the printed composite with a 90° raster angle and spooled composite filament, suggesting that the above-mentioned difference in electrical conductivity is due to the alignment of the nanofiller along the deposited filament. Such an alignment occurs within the nozzle during composite printing, as reported by other researchers [57,58]. This phenomenon is responsible for the increase in the electrical, mechanical, and thermal properties reported by other researchers [44,45,54]. In this study, the electrical conductivity passing from the spooled filament to the sample with a raster angle of 0° increased by approximately-two orders of magnitude. The electrical conductivity of the film specimen was of the same order of magnitude as that of the spooled filament. That is, the filler in the composite film is randomly orientated because no shear or elongational stress occurs, whereas the 3D-printing process orientates the filler along the direction of the deposition owing to the shear stresses applied to the material during the deposition phase. An appropriate configuration of electrical contacts results in a lower electrical resistance of the sample and, therefore, controlled anisotropy. Anisotropy in the electrical resistivity also determines anisotropy in the heat distribution, as observed for 3D-printed conductive graphene-doped PLA and pure PLA [59].

3.1.3. Correlation between the Joule heating behaviour and electrical anisotropy

In this study, the alignment of the nanofillers resulted in distinct anisotropic properties. These properties can contribute to a wide range of applications, including the thermal management of heat generation, according to which differentiated heating zones can be achieved by controlling the material structure/composition and the printing parameters (for example printing orientation). In particular, the electrical conductivity anisotropy of the printed materials described above verifies that they behaved as modulate-heating systems. Fig. 6(a, c) shows the electric heating behaviour of both printed composites (raster angles of 0 and 90°), considering a starting temperature of 27 °C. The applied voltage was very different for the two samples, namely, 45 and 170 V for the systems printed with raster angles of 0 and 90°, respectively. The temperature was detected by a thermocouple placed at the centre of the sample, as shown in Fig. 2(b, e).

All measurements were performed in ambient air to obtain similar boundary conditions on both surfaces of the printed samples acting as heaters (owing to the Joule effect of the current flowing through the sample). The temperature increased rapidly and linearly in the first stage until a steady-state temperature was reached, at which an almost equilibrium value was obtained. Similar temperature values (60–65 °C) were obtained by applying a significantly higher voltage to the composite printed with a raster angle of 90°. The temperature at the centre of the sample was almost the same over the entire surface of the sample if the edge effects are neglected, as observed in Fig. 6(b, d), which shows the thermal images for both systems after 20 min of heating, that is, under equilibrium conditions. A similar heating performance was expected because the two systems were characterised by different raster angles but exhibited the same void volume and similar thermal conductivity values over the entire heating range (see Table 3). The thermal conductivity was obtained in the direction normal to the XY surface (see Fig. 3(a)) along the thickness direction.

Furthermore, if the applied voltages and resistance values of the two samples are considered, the Joule heating results are similar. The power applied (P) is proportional to the generated heat, as shown in Eq. (2):

$$P = Q/t = RI^2 = V^2/R \quad (2)$$

where Q is the amount of heat, I is the electric current flowing through the conductor, V is the voltage applied across the conductor, R is the electrical resistance of the conductor, and t is the heating time. Therefore, similar applied power values cause similar heating phenomena. In this study, a power value of approximately 4 W was obtained (4.2 W for the composite with a raster angle of

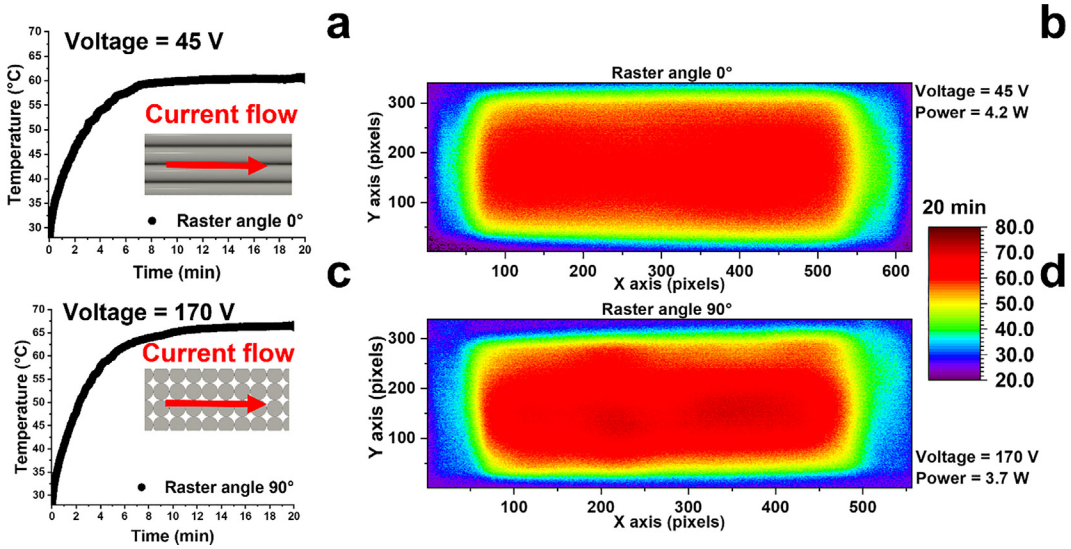

Fig. 6. (a) Temperature-time plot for the composite printed with a raster angle of 0° under an applied voltage of 45 V and (b) thermal image of the same sample after electric heating for 20 min. (c) Temperature-time plot for the composite printed with a raster angle of 90° under an applied voltage of 170 V and (d) thermal image of the same sample after electric heating of 20 min.

Table 3
Thermal conductivity of the 3D-printed composites at different temperatures.

Temperature (°C)	Thermal conductivity (W/mK) Raster angle 0°	Thermal conductivity (W/mK) Raster angle 90°
30.6	0.14	0.14
38.7	0.15	0.14
50.8	0.16	0.15
55.0	0.16	0.15
60.3	0.16	0.15
67.2	0.17	0.16

0° and 3.7 W for the composite with a raster angle of 90°), as shown in Fig. 6(b, d). The two systems were thermally equivalent and can be used as heating elements as long as the applied voltage is suitably modulated according to the chosen configuration.

Fig. 7 shows the local temperature in the central area of the printed composites under equilibrium conditions (after 20 min). The heating tests were performed at different applied voltages for both configurations. The almost homogeneous temperature maps clearly demonstrate that the composites effectively conducted heat. The homogeneity of the colour tone was translated into a unimodal temperature distribution for all applied voltage values. The narrow temperature distribution allows the voltage to be defined as a single technological parameter in heat management. The average temperature of the entire sample could be modulated by appropriately tuning the voltage (see Fig. 7(q, r)). Heating temperature values of 40–90 °C are suitable for many practical applications [60]. Materials such as ABS are generally applied well below their Tg (in the glassy state). The Tg of the CNT-based ABS is approximately 105 °C. This value was determined from the DSC curve, as described in Section 1.2. of S.I. section.

It can be deduced from the above-described behaviour that the anisotropic heating behaviour can be exploited to direct the heat generation only in some defined regions of the composite, which is easily feasible if a suitable combination or sequence of raster angles during the printing process is planned. Fig. 8(a) shows a schematic diagram of a composite (4.2 × 3.0 × 0.1 cm^3) obtained using a combination of the configurations shown in Fig. 2(a, d) (raster angle of 0° at the bottom and raster angle of 90° at the top). A voltage of 30 V was applied in the direction shown in Fig. 8(a).

As shown in Fig. 8(a), two thermocouples were positioned in the centre of the areas printed with raster angles of 0 and 90°. As expected, when the applied voltage was insufficient to induce effective heating in the region printed with a 90° raster angle (blue curve in Fig. 8(b)), the region of the composite printed with a 0° raster angle exhibited a temperature increase of approximately 30 °C. The thermal image in Fig. 8c, obtained after heating for 10 min, demonstrates the presence of a temperature gradient along the Y-axis of the surface of the analysed sample. The maximum value of the temperature gradient was 30 °C (see ΔT in Fig. 8(c)) at the centre of the sample and then this gradient decreased along the X-axis until it disappeared at the edges of the sample where the electrodes were applied. The temperature profiles were obtained in the two regions with different raster angles in the direction of the current flow, more precisely in the position marked by the Y-axis values of 100 pixels (centre of the region with a 0° raster angle) and 290 pixels (centre of the region with a 0° raster angle).

The obtained temperature difference (ΔT) could be tuned by varying the applied voltage. Fig. 9 shows the evolution of the thermal images of the sample for different voltage values.

An increase in the voltage resulted in a temperature difference of 50–55 °C (see Fig. 9(c)) within a few minutes (10 min) with a maximum temperature value of 80 °C in the 0°-oriented region, whereas the adjacent region of the sample printed with a raster angle of 90° exhibited a temperature of 30 °C. Different temperature values at different points on the sample can be planned by considering more complex printing configurations, such as those described below.

Fig. 10 shows a composite sample (0.35 × 9.00 × 1.50 cm^3) printed with three straight contour lines and a 45°-orientated filament in the central region, following a common design for 3D-printed objects, which is characterised by printing a straight-line patterned frame (raster angle of 0°) with diagonal deposition in the central part of the object. Two thermocouples were positioned to track the temperature trend in the different areas of the sample (one was placed on the contour area and the other in the centre of the sample).

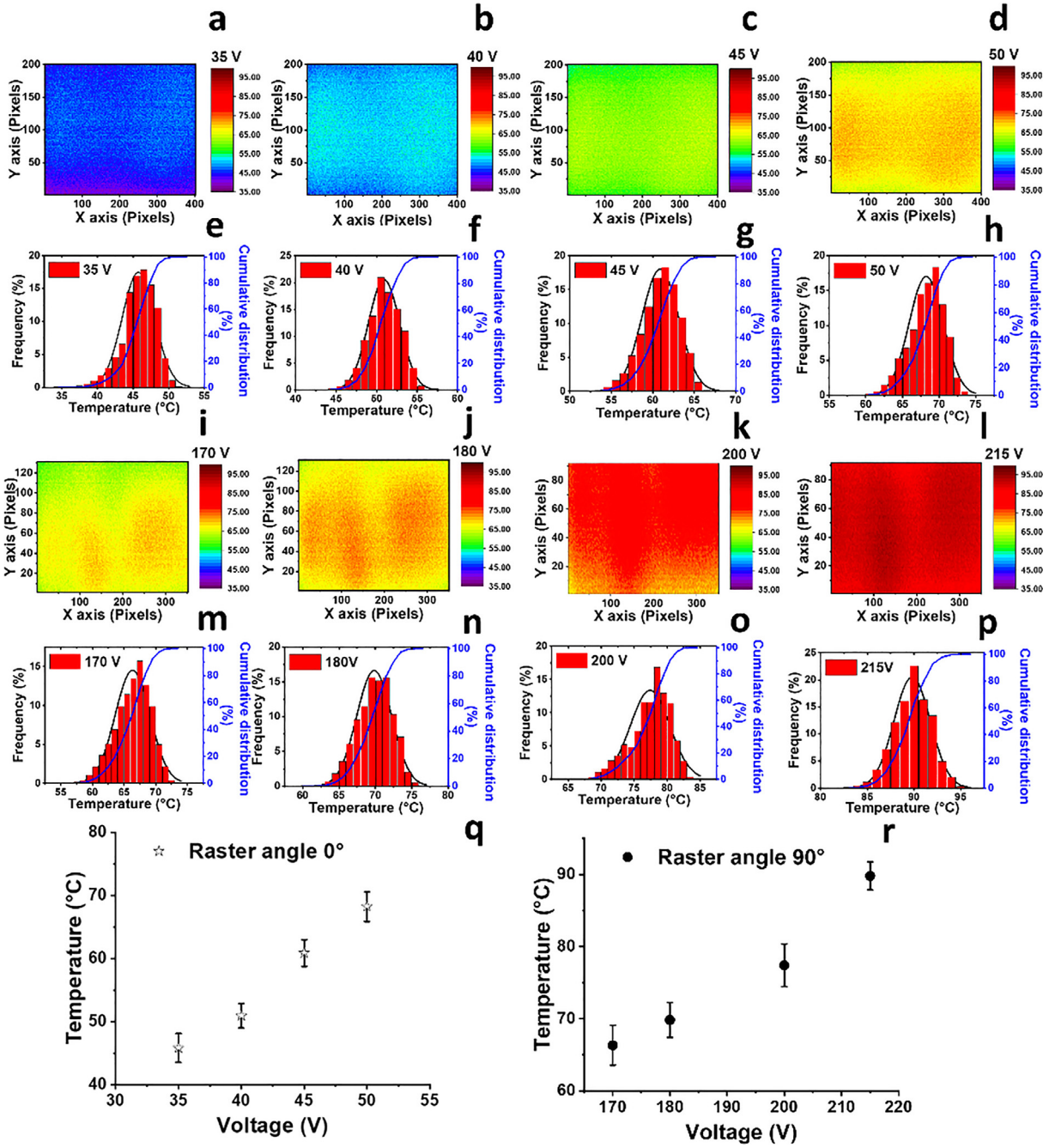

Fig. 7. Thermal images in the central region of the sample with a raster angle of 0° after a heating time of 20 min at (a) 35, (b) 40, (c) 45, and (d) 50 V. Temperature distributions of the sample printed with a raster angle of 0° at (e) 35, (f) 40, (g) 45, and (h) 50 V. Thermal images in the central region of the sample with a raster angle of 90° after a heating time of 20 min at (i) 170, (j) 180, (k) 200, and (l) 215 V. Temperature distributions of the sample printed with a raster angle of 90° at (m) 170, (n) 180, (o) 200, and (p) 215. In the temperature distribution images, the solid black lines are fitted by normal distribution curves and the solid blue lines are cumulative distribution curves. Maximum temperature values reached after 20 min under different voltages for the samples (q) with a raster angle of 0° and (r) with a raster angle of 90°. (For interpretation of the references to colour in this figure legend, the reader is referred to the web version of this article.)

Fig. 10(b) shows that the central zone reached a steady-state of approximately 50 °C in less than 3 min at an applied power of 2 W, whereas the boundary exhibited temperatures > 70 °C. Similar to the sample with the 0°-90° zones, if the filaments are deposited in the direction of the current flow, the resistivity in that zone is lower than in the other zones, thus enhancing the current flow and heat generation in that zone. The thermal images at three different times (1, 3, and 20 min) shows that the heat generation followed the raster angle of 45° in the central region, exhibiting temperature profiles with higher values at the edges of the sample and with lower values in the central region.

3.2. Implications for the future

The selective heating of specific regions of a material or device component meets the pressing current requirements for materials with smart functions. Such smart functions may find practical applications in many fields. For example, recent developments in

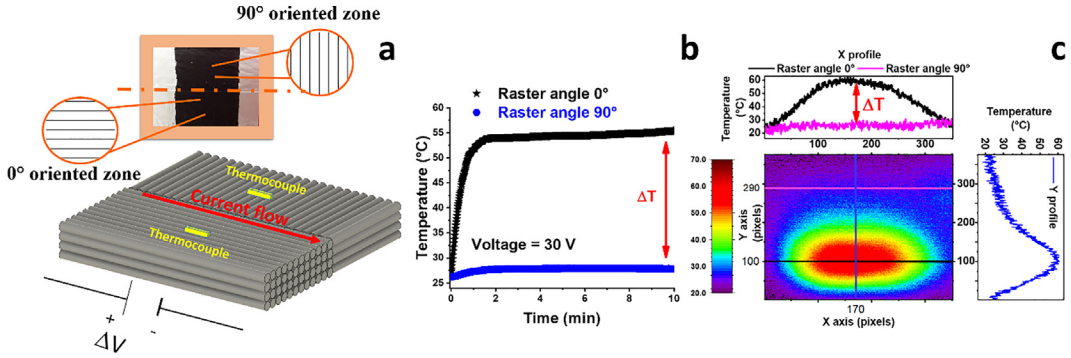

Fig. 8. (a) Configuration of the sample with a double raster angle combination (0 and 90°), (b) temperature–time plots for the system printed with a double raster combination under an applied voltage of 30 V, and (c) thermal image and temperature profile (X-axis and Y-axis) of the system printed with a double raster combination after electric heating for 10 min.

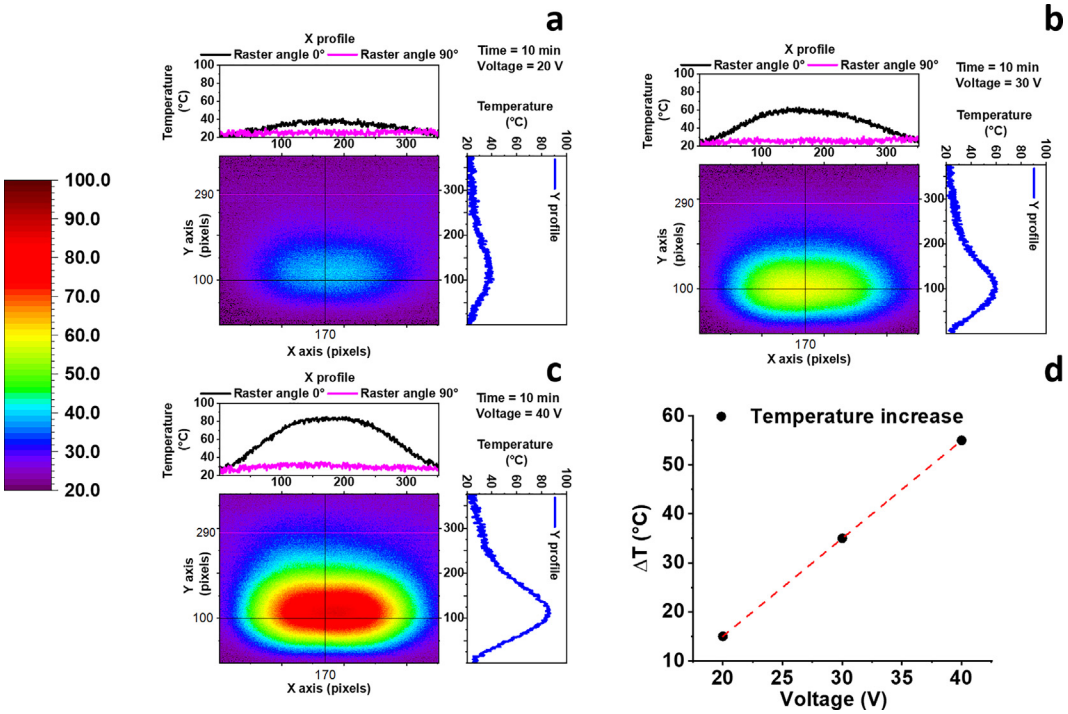

Fig. 9. Thermal images and temperature profiles (X-axis and Y-axis) of the system printed with a double raster angle combination after electric heating for 10 min under an applied voltage of (a) 20, (b) 30, and (c) 40 V. (d) Temperature difference (ΔT) between the sections printed with raster angles of 0 and 90° under different voltages.

robotic design refer to the need for flexible actuators activated by rapid localised heating. Lu *et al.* [61] described multilayer nanocomposites (MLN) with conductive carbon nanofibres for designing shape-memory materials capable of recovering their shape using the Joule heating effect. They found that a voltage of 30 V completely recovered the original shape of the MLN [61]. Selective heating only in regions dependent on motion is practical for plastic nanocomposites to avoid maintaining all parts at higher temperatures, which over time would incur faster physical and thermal degradation aging.

The same benefit can be achieved for the shape memory effect generated by shape memory alloys (SMAs) embedded into polymeric multilayer materials. In these systems, motion is activated by reversible shape memory effects due to crystallographic transitions (transformation between different crystallographic phases) induced by heating/cooling. The efficiency of the system motion requires setting and controlling the temperature of the polymer embedding the metal alloy, which is in the form of wires or other geometric shapes. Selective temperature control restricted only to the polymeric part in contact with the SMA component is highly desirable to preserve the integrity of the bulk polymeric material without affecting the efficiency of the specific functionality. Recently the need for a strategy to minimise the effects of adverse weather conditions on the capacity decay rate of batteries was discussed [60]. Lightweight heated polymeric containers allow the battery life to be extended during periods of intense cold or in geographic areas with temperatures close to or below 0 °C. The battery container can be designed to localise heat only on the surface that is in contact with the battery. Generally, printed polymers that integrate the smart function to selectively heat only limited regions of the sample can be advantageously applied in many cases where heating is realised without cutting or compromising the integrity of the polymeric material/component (for example, in the form of layers).

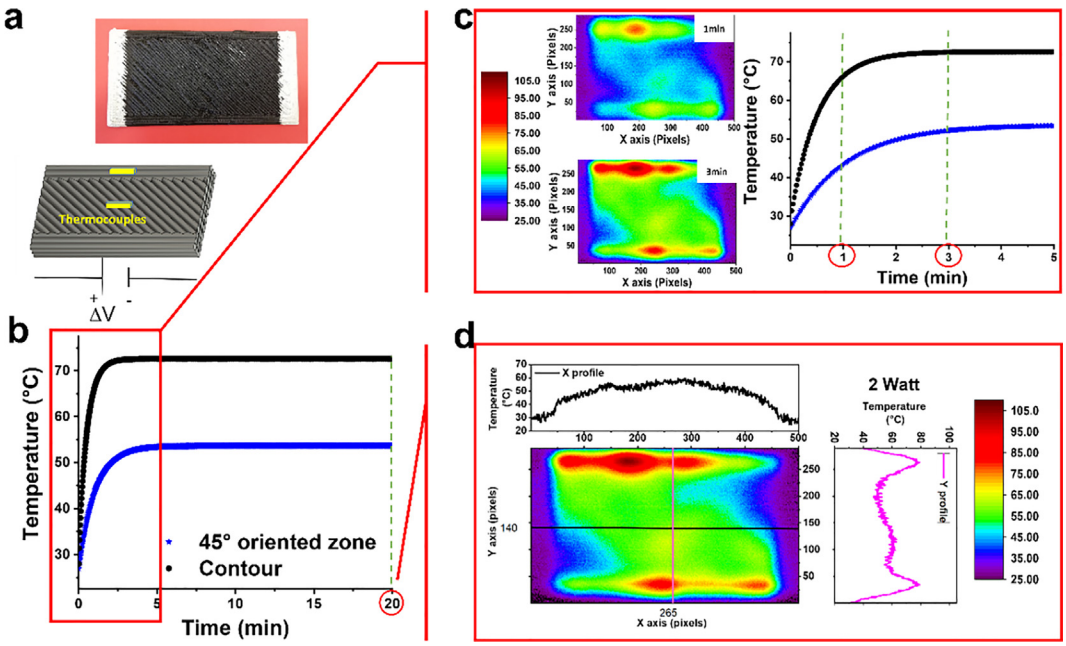

Fig. 10. (a) Schematic diagram of the configuration of the sample with a double raster angle combination (0° at the edges and 45° in the central region), (b) temperature–time plots at an applied power of 2 W, (c) thermal image and temperature–time plot of the system during the first 5 min, and (d) thermal image and temperature profile (X-axis and Y-axis) of the system after electric heating for 20 min.

4. Conclusions

This paper presents an experimental study on the electrical and thermal properties of FFF 3D-printed composites based on ABS with MWCNTs. They were manufactured by varying their configurations using the printing parameters, such that different conductive behaviours were obtained. These differences were attributed to changes in the conductive nanometric network formed within the polymeric material. Atomic force microscopy (AFM) in the TUNA modality was used to investigate the morphology of 3D printed parts, which allowed direct information on the electrically conductive paths to be obtained. The experimental results showed that a suitable choice of printing parameters allows for the electrothermal conduction paths to be controlled, and consequently, the temperature in the different zones of the printed samples could be controlled. Hence, it was demonstrated that the different parts of a system could be heated in a controlled manner by exploiting the anisotropy in the electrical resistivity values of the 3D-printed parts. Additionally, the raster angle was the dominant factor for altering the electrical conductivity of the parts. The electrical and thermal anisotropy can be determined at the design stage by suitably choosing the texture and, therefore, the conductive paths of the 3D-printed samples. These observations open a range of possibilities. For example, different raster angles can be applied to different layers such that one of the sample surfaces exhibits a high temperature and the other surface remains very close to room temperature. Furthermore, by suitably modulating the electrical signal, it is possible to design devices that operate at values close to the corresponding steady-state conditions.

CRediT authorship contribution statement

Liberata Guadagno: Writing – review & editing, Supervision, Project administration, Funding acquisition. **Francesca Aliberti:** Investigation, Data curation, Visualization. **Raffaele Longo:** Investigation, Data curation, Visualization. **Marialuigia Raimondo:** Investigation, Data curation, Visualization. **Roberto Pantani:** Writing – review & editing. **Andrea Sorrentino:** Formal analysis, Investigation, Resources. **Michelina Catauro:** Writing – review & editing. **Luigi Vertuccio:** Conceptualization, Methodology, Writing – original draft, Writing – review & editing.

Data availability

Data will be made available on request.

Declaration of Competing Interest

The authors declare that they have no known competing financial interests or personal relationships that could have appeared to influence the work reported in this paper.

Appendix A. Supplementary material

Supplementary data to this article can be found online at https://doi.org/10.1016/j.matdes.2022.111507.

References

[1] F. Rengier, A. Mehndiratta, H. Von Tengg-Kobligk, C.M. Zechmann, R. Unterhinninghofen, H.U. Kauczor, F.L. Giesel, 3D printing based on imaging data: review of medical applications, Int. J. Comput. Assist. Radiol. Surg. 54 (5) (2010), https://doi.org/10.1007/S11548-010-0476-X.
[2] N.W. Solís Pinargote, A. Smirnov, N. Peretyagin, A. Seleznev, P. Peretyagin, Direct ink writing technology (3D printing) of graphene-based ceramic nanocomposites: a review, Nanomaterials 10 (7) (2020) 1300.
[3] J.T. Muth, D.M. Vogt, R.L. Truby, Y. Mengüç, D.B. Kolesky, R.J. Wood, J.A. Lewis, Embedded 3D printing of strain sensors within highly stretchable elastomers, Adv. Mater. 26 (2014) 6307–6312, https://doi.org/10.1002/ADMA.201400334.
[4] S. Pan, J. Yuan, T. Zheng, Z. She, X. Li, Interfacial thermal conductance of in situ aluminum-matrix nanocomposites, J. Mater. Sci. 56 (2021) 13646–13658, https://doi.org/10.1007/S10853-021-06176-7/FIGURES/11.
[5] S. Pan, T. Wang, K. Jin, X. Cai, Understanding and designing metal matrix nanocomposites with high electrical conductivity: a review, J. Mater. Sci. 5712 (57) (2022), https://doi.org/10.1007/S10853-022-07010-4.
[6] S. Pan, J. Yuan, P. Zhang, M. Sokoluk, G. Yao, X. Li, Effect of electron concentration on electrical conductivity in in situ Al-TiB2 nanocomposites, Appl. Phys. Lett. 116 (1) (2020) 014102.

[7] I. Momohjimoh, N. Saheb, M.A. Hussein, T. Laoui, N. Al-Aqeeli, Electrical conductivity of spark plasma sintered Al2O3–SiC and Al2O3-carbon nanotube nanocomposites, Ceram. Int. 46 (2020) 16008–16019, https://doi.org/10.1016/J.CERAMINT.2020.03.151.
[8] E. Kroll, D. Artzi, Enhancing aerospace engineering students' learning with 3D printing wind-tunnel models, Rapid Prototyp. J. 17 (2011) 393–402, https://doi.org/10.1108/13552541111156522.
[9] F. Mami, J.P. Revéret, S. Fallaha, M. Margni, Evaluating eco-efficiency of 3D printing in the aeronautic industry, J. Ind. Ecol. 21 (2017) S37–S48, https://doi.org/10.1111/JIEC.12693.
[10] P. Costa, J.R. Dios, J. Cardoso, J.J. Campo, C.R. Tubio, B.F. Gonçalves, N. Castro, S. Lanceros-Méndez, Polycarbonate based multifunctional self-sensing 2D and 3D printed structures for aeronautic applications, Smart Mater. Struct. 30 (8) (2021) 085032.
[11] Z. Weng, J. Wang, T. Senthil, L. Wu, Mechanical and thermal properties of ABS/montmorillonite nanocomposites for fused deposition modeling 3D printing, Mater. Des. 102 (2016) 276–283, https://doi.org/10.1016/J.MATDES.2016.04.045.
[12] Y. Ming, Y. Duan, S. Zhang, Y. Zhu, B. Wang, Self-heating 3D printed continuous carbon fiber/epoxy mesh and its application in wind turbine deicing, Polym. Test. 82 (2020), https://doi.org/10.1016/J.POLYMERTESTING.2019.106309 106309.
[13] A. Riaz, P. Töllner, A. Ahrend, A. Springer, B. Milkereit, H. Seitz, Optimization of composite extrusion modeling process parameters for 3D printing of low-alloy steel AISI 8740 using metal injection moulding feedstock, Mater. Des. 219 (2022), https://doi.org/10.1016/J.MATDES.2022.110814 110814.
[14] B.C. Gross, J.L. Erkal, S.Y. Lockwood, C. Chen, D.M. Spence, Evaluation of 3D printing and its potential impact on biotechnology and the chemical sciences, Anal. Chem. 86 (2014) 3240–3253, https://doi.org/10.1021/AC403397R/ASSET/IMAGES/LARGE/AC-2013-03397R_0009.JPEG.
[15] S.V. Murphy, A. Atala, 3D bioprinting of tissues and organs, Nat. Biotechnol. 328 (32) (2014) 773–785, https://doi.org/10.1038/nbt.2958.
[16] M. Touri, F. Kabirian, M. Saadati, S. Ramakrishna, M. Mozafari, Additive manufacturing of biomaterials – the evolution of rapid prototyping, Adv. Eng. Mater. 21 (2019) 1800511, https://doi.org/10.1002/ADEM.201800511.
[17] D. Aki, S. Ulag, S. Unal, M. Sengor, N. Ekren, C.C. Lin, H. Yılmazer, C.B. Ustundag, D.M. Kalaskar, O. Gunduz, 3D printing of PVA/hexagonal boron nitride/bacterial cellulose composite scaffolds for bone tissue engineering, Mater. Des. 196 (2020), https://doi.org/10.1016/J.MATDES.2020.109094 109094.
[18] X. Bi, R. Huang, 3D printing of natural fiber and composites: a state-of-the-art review, Mater. Des. 222 (2022), https://doi.org/10.1016/J.MATDES.2022.111065 111065.
[19] C. Yuan, F. Wang, B. Qi, Z. Ding, D.W. Rosen, Q. Ge, 3D printing of multi-material composites with tunable shape memory behavior, Mater. Des. 193 (2020), https://doi.org/10.1016/J.MATDES.2020.108785 108785.
[20] C.F. Du, Q. Liang, Y. Luo, Y. Zheng, Q. Yan, Recent advances in printable secondary batteries, J. Mater. Chem. A. 5 (2017) 22442–22458, https://doi.org/10.1039/C7TA07856K.
[21] Y. Wang, Z.W. Fan, H. Zhang, J. Guo, D.X. Yan, S. Wang, K. Dai, Z.M. Li, 3D-printing of segregated carbon nanotube/polylactic acid composite with enhanced electromagnetic interference shielding and mechanical performance, Mater. Des. 197 (2021), https://doi.org/10.1016/J.MATDES.2020.109222 109222.
[22] E. Ivaniuk, M. Friedrich Eichenauer, Z. Tošić, S. Müller, D. Lordick, V. Mechtcherine, 3D printing and assembling of frame modules using printable strain-hardening cement-based composites (SHCC), Mater. Des. 219 (2022), https://doi.org/10.1016/J.MATDES.2022.110757 110757.
[23] J.P. Jose, S. Thomas, J. Kuruvilla, S.K. Malhotra, K. Goda, M.S. Sreekala, Advances in polymer composites: macro- and microcomposites – state of the art, new challenges, and opportunities, Polym. Compos. 1 (2012), https://doi.org/10.1002/9783527645213.
[24] L. Guadagno, A. Sorrentino, P. Delprat, L. Vertuccio, Design of Multifunctional Composites: New Strategy to Save Energy and Improve Mechanical Performance, Nanomater. 10 (2020) 2285, doi: 10.3390/NANO10112285.
[25] L. Vertuccio, L. Guadagno, G. Spinelli, P. Lamberti, M. Zarrelli, S. Russo, G. Iannuzzo, Smart coatings of epoxy based CNTs designed to meet practical expectations in aeronautics, Compos. Part B Eng. 147 (2018) 42–46, https://doi.org/10.1016/J.COMPOSITESB.2018.04.027.
[26] L. Vertuccio, L. Guadagno, G. Spinelli, S. Russo, G. Iannuzzo, Effect of carbon nanotube and functionalized liquid rubber on mechanical and electrical properties of epoxy adhesives for aircraft structures, Compos. Part B Eng. 129 (2017) 1–10, https://doi.org/10.1016/J.COMPOSITESB.2017.07.021.
[27] L. Guadagno, M. Raimondo, L. Vertuccio, C. Naddeo, G. Barra, P. Longo, P. Lamberti, G. Spinelli, M.R. Nobile, Morphological, rheological and electrical properties of composites filled with carbon nanotubes functionalized with 1-pyrenebutyric acid, Compos. Part B Eng. 147 (2018) 12–21, https://doi.org/10.1016/J.COMPOSITESB.2018.04.036.
[28] L. Vertuccio, S. Russo, M. Raimondo, K. Lafdi, L. Guadagno, Influence of carbon nanofillers on the curing kinetics of epoxy-amine resin, (2015), doi: 10.1039/c5ra14343h.
[29] X. Wang, M. Jiang, Z. Zhou, J. Gou, D. Hui, 3D printing of polymer matrix composites: a review and prospective, Compos. Part B Eng. 110 (2017) 442–458, https://doi.org/10.1016/J.COMPOSITESB.2016.11.034.
[30] S. Drücker, H. Voormann, K.P. von Berg, M.W.H. Ahrens, V.K. Wisniewski, E. Schröder, A. Kehne, S. Detjen, S. Kaysser, C.A. Keun, B. Fiedler, Solid epoxy for functional 3D printing with isotropic mechanical properties by material extrusion, Addit. Manuf. 55 (2022), https://doi.org/10.1016/J.ADDMA.2022.102797 102797.
[31] J.M. Gardner, G. Sauti, J.W. Kim, R.J. Cano, R.A. Wincheski, C.J. Stelter, B.W. Grimsley, D.C. Working, E.J. Siochi, 3-D printing of multifunctional carbon nanotube yarn reinforced components, Addit. Manuf. 12 (2016) 38–44, https://doi.org/10.1016/J.ADDMA.2016.06.008.
[32] Y. Shmueli, Y.C. Lin, X. Zuo, Y. Guo, S. Lee, G. Freychet, M. Zhernenkov, T. Kim, R. Tannenbaum, G. Marom, D. Gersappe, M.H. Rafailovich, In-situ X-ray scattering study of isotactic polypropylene/graphene nanocomposites under shear during fused deposition modeling 3D printing, Compos. Sci. Technol. 196 (2020), https://doi.org/10.1016/J.COMPSCITECH.2020.108227 108227.
[33] D. Ponnamma, Y. Yin, N. Salim, J. Parameswaranpillai, S. Thomas, N. Hameed, Recent progress and multifunctional applications of 3D printed graphene nanocomposites, Compos. Part B Eng. 204 (2021), https://doi.org/10.1016/J.COMPOSITESB.2020.108493 108493.
[34] F. Ning, W. Cong, J. Qiu, J. Wei, S. Wang, Additive manufacturing of carbon fiber reinforced thermoplastic composites using fused deposition modeling, Compos. Part B Eng. 80 (2015) 369–378, https://doi.org/10.1016/J.COMPOSITESB.2015.06.013.
[35] X. Wei, D. Li, W. Jiang, Z. Gu, X. Wang, Z. Zhang, Z. Sun, 3D printable graphene composite, Sci. Rep. 5 (1) (2015).
[36] A. Maurel, M. Courty, B. Fleutot, H. Tortajada, K. Prashantha, M. Armand, S. Grugeon, S. Panier, L. Dupont, Highly loaded graphite-polylactic acid composite-based filaments for lithium-ion battery three-dimensional printing, Chem. Mater. 30 (2018) 7484–7493, https://doi.org/10.1021/ACS.CHEMMATER.8B02062/ASSET/IMAGES/LARGE/CM-2018-020625_0006.JPEG.
[37] K. Prashantha, F. Roger, Multifunctional properties of 3D printed poly(lactic acid)/graphene nanocomposites by fused deposition modeling, 54 (2016) 24–29, doi: 10.1080/10601325.2017.1250311.
[38] C.B. Sweeney, B.A. Lackey, M.J. Pospisil, T.C. Achee, V.K. Hicks, A.G. Moran, B.R. Teipel, M.A. Saed, M.J. Green, Welding of 3D-printed carbon nanotube–polymer composites by locally induced microwave heating, Sci. Adv. 3 (2017), https://doi.org/10.1126/SCIADV.1700262/SUPPL_FILE/1700262_SM.PDF.
[39] X. Tian, T. Liu, C. Yang, Q. Wang, D. Li, Interface and performance of 3D printed continuous carbon fiber reinforced PLA composites, Compos. Part A Appl. Sci. Manuf. 88 (2016) 198–205, https://doi.org/10.1016/J.COMPOSITESA.2016.05.032.
[40] G. Spinelli, P. Lamberti, V. Tucci, R. Kotsilkova, E. Ivanov, D. Menseidov, C. Naddeo, V. Romano, L. Guadagno, R. Adami, D. Meisak, D. Bychanok, P. Kuzhir, Nanocarbon/poly(lactic) acid for 3D printing: effect of fillers content on electromagnetic and thermal properties, Mater. 12 (2019) 2369, doi: 10.3390/MA12152369.
[41] C.Y. Foo, H.N. Lim, M.A. Mahdi, M.H. Wahid, N.M. Huang, Three-dimensional printed electrode and its novel applications in electronic devices, Sci. Rep. 8 (1) (2018).
[42] A.K. Sood, R.K. Ohdar, S.S. Mahapatra, Parametric appraisal of mechanical property of fused deposition modelling processed parts, Mater. Des. 31 (2010) 287–295, https://doi.org/10.1016/J.MATDES.2009.06.016.
[43] N. Nguyen, J.G. Park, S. Zhang, R. Liang, Recent advances on 3D printing technique for thermal-related applications, Adv. Eng. Mater. 20 (2018) 1700876, https://doi.org/10.1002/ADEM.201700876.
[44] Y. Jia, H. He, Y. Geng, B. Huang, X. Peng, High through-plane thermal conductivity of polymer based product with vertical alignment of graphite flakes achieved via 3D printing, Compos. Sci. Technol. 145 (2017) 55–61, https://doi.org/10.1016/J.COMPSCITECH.2017.03.035.
[45] D. Zhu, Y. Ren, G. Liao, S. Jiang, F. Liu, J. Guo, G. Xu, Thermal and mechanical properties of polyamide 12/graphene nanoplatelets nanocomposites and parts fabricated by fused deposition modeling, J. Appl. Polym. Sci. 134 (2017) 45332, https://doi.org/10.1002/APP.45332.
[46] H.J. Kim, D.E. Kim, MD simulation of the frictional behavior of CNTs with respect to orientation, Tribol. Int. 50 (2012) 51–56, https://doi.org/10.1016/J.TRIBOINT.2012.01.007.
[47] M. Dong, J. Zhang, G. Hou, L. Liu, X. Qu, Y. Yu, C. Yuan, X. Wang, Thermal conductivity of GP/ZnO@CNTs nanocomposites improved greatly by orientation of CNTs under shear field, Compos. Commun. 17 (2020) 61–65, https://doi.org/10.1016/J.COCO.2019.11.010.
[48] S. Dul, B.J.A. Gutierrez, A. Pegoretti, J. Alvarez-Quintana, L. Fambri, 3D printing of ABS Nanocomposites. Comparison of processing and effects of multi-wall and single-wall carbon nanotubes on thermal, mechanical and electrical properties, J. Mater. Sci. Technol. 121 (2022) 52–66, https://doi.org/10.1016/J.JMST.2021.11.064.
[49] N. Vidakis, M. Petousis, E. Velidakis, L. Tzounis, N. Mountakis, O. Boura, S.A. Grammatikos, Multi-functional polyamide 12 (PA12)/ multiwall carbon nanotube 3D printed nanocomposites with enhanced mechanical and electrical properties, Adv. Compos. Mater 31 (6) (2022) 630–654.
[50] N. Vidakis, M. Petousis, M. Kourinou, E. Velidakis, N. Mountakis, P.E. Fischer-Griffiths, S. Grammatikos, L. Tzounis, Additive manufacturing of multifunctional polylactic acid (PLA)—multiwalled carbon nanotubes (MWCNTs) nanocomposites, Nanocomposites 7 (1) (2021) 184–199.
[51] A.T. Chien, S. Cho, Y. Joshi, S. Kumar, Electrical conductivity and Joule heating of polyacrylonitrile/carbon nanotube composite fibers, Polymer (Guildf). 55 (2014) 6896–6905, https://doi.org/10.1016/J.POLYMER.2014.10.064.
[52] Z. Sang, Q. Zhou, K. Kumar Rajagopalan, E.L. Thomas, F. Gardea, S.A. Sukhishvili, Dynamic polymer network conductive Nanocomposites: low percolation threshold and Joule-heating-induced network plasticity, Chem. Eng. J. 443 (2022), https://doi.org/10.1016/J.CEJ.2022.136400 136400.

[53] B. Micó-Vicent, E. Perales, K. Huraibat, F.M. Martínez-Verdú, V. Viqueira, Maximization of FDM-3D-objects gonio-appearance effects using PLA and ABS filaments and combining several printing parameters: "A case study", Materials (Basel) 12 (9) (2019) 1423.
[54] H.K. Sezer, O. Eren, FDM 3D printing of MWCNT re-inforced ABS nano-composite parts with enhanced mechanical and electrical properties, J. Manuf. Process. 37 (2019) 339–347, https://doi.org/10.1016/J.JMAPRO.2018.12.004.
[55] G. Spinelli, P. Lamberti, V. Tucci, L. Guadagno, L. Vertuccio, Damage monitoring of structural resins loaded with carbon fillers: experimental and theoretical study, Nanomaterials 10 (3) (2020) 434.
[56] L. Vertuccio, F. Foglia, R. Pantani, M.D. Romero-Sánchez, B. Calderón, L. Guadagno, Carbon nanotubes and expanded graphite based bulk nanocomposites for de-icing applications, Compos. Part B Eng. 207 (2021), https://doi.org/10.1016/J.COMPOSITESB.2020.108583 108583.
[57] B.G. Compton, J.A. Lewis, 3D-printing of lightweight cellular composites, Adv. Mater. 26 (2014) 5930–5935, https://doi.org/10.1002/ADMA.201401804.
[58] G.D. Goh, Y.L. Yap, S. Agarwala, W.Y. Yeong, Recent progress in additive manufacturing of fiber reinforced polymer composite, Adv. Mater. Technol. 4 (2019) 1800271, https://doi.org/10.1002/ADMT.201800271.
[59] Y. Zhuang, W. Song, G. Ning, X. Sun, Z. Sun, G. Xu, B. Zhang, Y. Chen, S. Tao, 3D–printing of materials with anisotropic heat distribution using conductive polylactic acid composites, Mater. Des. 126 (2017) 135–140, https://doi.org/10.1016/J.MATDES.2017.04.047.
[60] L. Guadagno, L. Vertuccio, F. Foglia, M. Raimondo, G. Barra, A. Sorrentino, R. Pantani, E. Calabrese, Flexible eco-friendly multilayer film heaters, Compos. Part B Eng. 224 (2021), https://doi.org/10.1016/J.COMPOSITESB.2021.109208 109208.
[61] H. Lu, F. Liang, Y. Yao, J. Gou, D. Hui, Self-assembled multi-layered carbon nanofiber nanopaper for significantly improving electrical actuation of shape memory polymer nanocomposite, Compos. Part B Eng. 59 (2014) 191–195, https://doi.org/10.1016/J.COMPOSITESB.2013.12.009.